Coherent multi-pulsing induced by engineered heterogeneity in diode laser arrays

Greggory Scranton[1], Kendall Golden[2], Olivier Spitz[1,*], Arindam Mishra[1], Igor Belykh[2,†], and Yehuda Braiman[1,3,‡]

[1]The College of Optics and Photonics (CREOL), University of Central Florida, Orlando, FL 32816, USA
[2]Department of Mathematics and Statistics and Neuroscience Institute, Georgia State University, P.O. Box 4110, Atlanta, Georgia, 30302-410, USA
[3]Department of Electrical and Computer Engineering, University of Central Florida, Orlando, FL 32816, USA
[*]olivier.spitz@ucf.edu
[†]ibelykh@gsu.edu
[‡]yehuda.braiman@ucf.edu

ABSTRACT

The generation of high-power controlled pulse trains in semiconductor lasers is of significant theoretical and practical interest, with broad applications across many fields. Previous work on diode lasers has primarily focused on single-pulse emission from individual diodes, inherently limiting output power. Here, we demonstrate that large direct-current-driven external-cavity laser arrays, subject only to optical feedback and engineered frequency heterogeneity, can exhibit robust, coherent multi-pulsing dynamics. We uncover a multi-pulse generation mechanism driven by two-cluster formation and heterogeneity-induced interburst oscillations, resulting in desirable features such as multi-GHz operation, high peak power, and nearly perfect phase synchronization. Our results pave the way for designing and manufacturing miniature photonic chip arrays capable of scalable multi-pulse generation. Beyond photonics, the underlying multi-pulse mechanism may be broadly relevant to physical and biological networks, where oscillator heterogeneity can give rise to coherent spiking and bursting dynamics.

Introduction

Semiconductor lasers are well known for their excitability under various perturbations that disrupt steady-state operation, with pulsing dynamics playing a crucial role in applications such as optical neurons[1,2] and photonic processors[3]. Most prior studies have focused on single-laser systems, where controllable pulsing typically requires external mechanisms such as AC driving[4], strong current modulation[5,6], or unilateral injection[7–9]. These approaches can generate short pulses, including gain-switched and mode-locked pulses down to picoseconds[10–13], often aided by saturable absorbers[14]. However, these external methods are difficult to scale, and extending synchronized pulsing to large arrays remains elusive. Numerical studies of arrays with saturable absorbers have demonstrated pulsing, but the pulses tend to propagate spatially rather than synchronize across emitters[15–17], limiting coherent emission and power scaling[18]. Configurations with two lasers subject to both transverse coupling and optical feedback showed limited success in achieving synchronous pulsing[19,20], but larger implementations have not exhibited robust collective pulsing[19,21], and approaches using incoherent feedback[22] remain largely unexplored for scalable array synchronization. Thus, despite advances in pulse generation techniques, achieving robust, synchronized multi-pulse emission across large semiconductor laser arrays without extensive active control remains a critical and open challenge.

Meanwhile, synchronization of oscillatory dynamics in laser arrays has been extensively studied[23–37], with intrinsic heterogeneity and noise often regarded as disruptive factors. However, since the discovery that disorder can tame spatiotemporal instabilities and induce synchronization in oscillator networks[38,39], it has been shown, both theoretically and experimentally, that under certain conditions, disorder-induced synchronization and coherent dynamics can emerge across a wide range of physical and engineering systems[40–47]. Notably, it has been demonstrated that a time-delayed laser array with inherent heterogeneity, composed of broad-area diodes in an external V-shaped cavity, under the right conditions can achieve perfect synchrony[48,49]. Specifically, while frequency heterogeneity typically degrades phase synchrony, the introduction of misalignment (heterogeneity in time delays) can completely reverse this effect, leading to nearly perfect phase-synchronized behavior[50].

In this work, we address the long-standing challenge of synchronizing single pulsing and, more critically, the inherently difficult multi-pulse dynamics in large semiconductor laser arrays, a major bottleneck in high-power optical pulse generation. We demonstrate that large arrays of semiconductor lasers subject to optical feedback and non-local delayed coupling can exhibit robust, high-power, coherent, and periodic pulsing dynamics at multi-GHz frequencies. This coherent pulsing is induced

by an engineered frequency-detuning heterogeneity among time-delayed coupled emitters, offering a robust and effective pathway for generating synchronized multi-pulse dynamics. The resulting pulses exhibit narrow widths of tens of picoseconds, tunable intervals between well-separated single and multi-spike trains, and transitions from anti-phase to in-phase locking—key features for coherent beam combining. Notably, the single- and multi-pulse regimes we report occur in parameter regions where the array operates near a fixed-point solution, i.e., with nearly constant intensity and carrier density in the absence of pulsing. This regime typically corresponds to high injection currents, often several times the threshold current, resulting in high-intensity emitted pulses. By designing the detuning pattern to alternate between odd and even-numbered lasers, we effectively partition the array into two clusters that pulse out of phase with each other. The timing between the oscillations of these clusters introduces a slow modulation superimposed on the fast pulsing dynamics, resulting in a rich temporal structure. Specifically, the overall periodicity of the pulse trains reflects the external cavity round-trip time, plus an additional inter-cluster timing offset governed by the detuning arrangement. As a result, the system exhibits multiple intrinsic time scales: the cavity round-trip time, the inter-cluster delay, and the intra-train pulse spacing. Importantly, the amplitude of pulses within each train remains nearly constant, indicating that these dynamics are distinct from relaxation oscillations. The number of pulses per train depends sensitively on how closely the system operates near the fixed-point regime, and we quantify this dependence across key array parameters. Furthermore, due to the multistability inherent in the system, small perturbations, when properly directed, can induce transitions between different multi-pulse states, each characterized by a distinct pulse count and temporal spacing. We note that the multi-pulse generation mechanism is specific to laser arrays and cannot be realized with a solitary single laser. Remarkably, however, many features of the multi-pulse behavior observed in large arrays with engineered frequency detunings can already be qualitatively captured in a system of just two coupled lasers, providing valuable insights into the underlying generation mechanisms. These findings highlight not only the robustness of the pulsing regime but also its high degree of tunability and controllability through passive structural parameters.

Unlike prior studies on single-pulse dynamics, which begin with simplified representations such as the Adler model[51,52] or the Ginzburg-Landau equations[53], our work is grounded entirely in the realistic and widely used Lang-Kobayashi laser array framework. Despite their significance as theoretical tools for exploring pulsing dynamics, these earlier models lack a direct connection to the physical equations governing semiconductor lasers and were unable to exhibit coherent multi-pulse regimes. Using analytical techniques and numerical simulations, we uncover the underlying mechanism of pulse generation in Lang-Kobayashi laser arrays and demonstrate that certain, possibly broad, distributions of intrinsic laser frequencies lead to the emergence of a two-cluster coherent state that supports both single-pulse and multi-pulse regimes. To accurately predict the parameter space of interest for pulsing within the Lang-Kobayashi model, we further develop a reduced model that reveals an emergent frequency of interburst oscillations and relates it to the number of pulses per unit time, which is close to the cavity round-trip time. This mechanism enables controllable, coherent multi-pulsing dynamics, distinct from the conventional saddle-node bifurcation on an invariant circle (SNIC) that yields only single-pulse solutions[54] observed in the classical time-delayed Adler equation and termed topological solitons[51–53,55]. Our findings demonstrate the potential of all-optical pulsing in large laser arrays, offering a scalable route for phase-locked beam combining and enhanced optical power delivery.

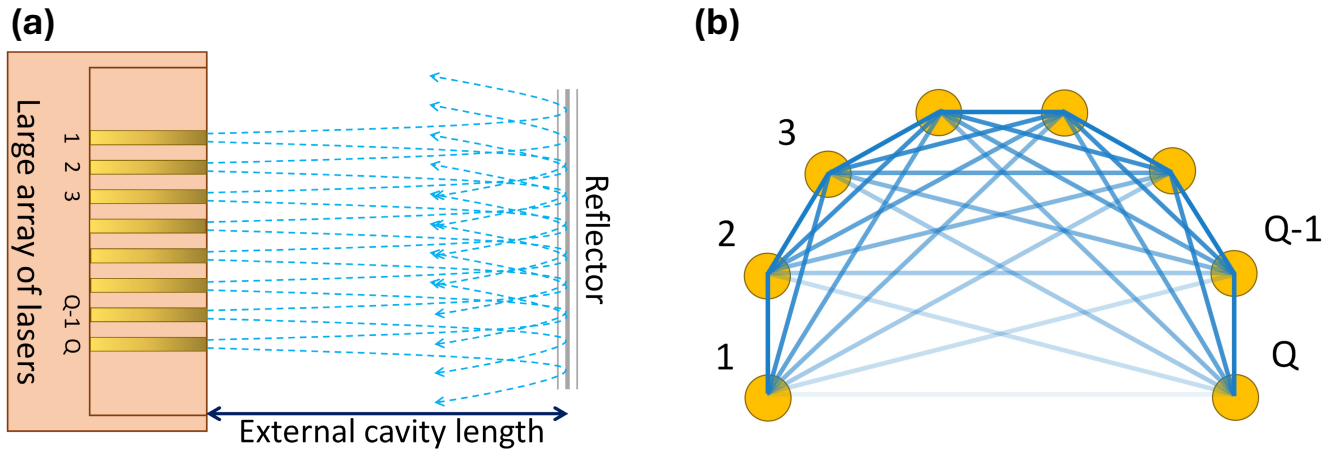

Figure 1. (a) Array of semiconductor lasers subject to decayed non-local coupling and optical feedback. The external reflector provides the feedback and decayed coupling. The reflected beam from each emitter couples to the other lasers in the array after a time delay τ. (b) The equivalent network of emitters with decayed non-local coupling. The transparency of the links is inversely proportional to the coupling strength between emitters. $Q = 30$ for simulations shown in Figs. 2-3.

Results

Laser array model

We consider a large array of Q delay-coupled semiconductor lasers with decayed non-local coupling described by a version[50] of the Lang-Kobayashi equations[56]:

$$\begin{aligned}\dot{E}_q(t) &= \tfrac{1+i\alpha}{2}\left(g\tfrac{N_q(t)-N_0}{1+s|E_q(t)|^2}-\gamma\right)E_q(t)+i\omega_q E_q(t)+\tfrac{\kappa^f}{Q}\sum_{j=1}^{Q}A_{qj}E_j(t-\tau)\\ \dot{N}_q(t) &= \beta J_{th}-\gamma_n N_q(t)-g\tfrac{N_q(t)-N_0}{1+s|E_q(t)|^2}|E_q(t)|^2,\end{aligned} \tag{1}$$

with the qth laser complex field $E_q(t)=r_q(t)\exp i\phi_q(t)$ and carrier number $N_q(t)$. The parameters are customary for Lang-Kobayashi-type models: g and N_0 are the differential gain coefficient and number of carriers at transparency, respectively, γ is the cavity loss rate, $J_{th}=\gamma_n[N_0+(\gamma/g)]$ is the pump current threshold, the pump factor $\beta>1$ means that the lasers are biased above threshold, γ_n is the carrier loss rate, κ^f is the feedback strength. The frequency detuning of the qth laser is ω_q. The time delay τ is the external cavity round-trip time, which is identical for all lasers. $A_{qj}=d^{|q-j|}\in(0,1)$ is the entry of the decay non-local coupling matrix connecting the qth laser to the jth laser. Although we have computationally verified the emergence of pulses even in the presence of noise and/or non-identical time delays, we have not considered noise and misalignment heterogeneities here in order to explain the pulsing mechanism better and facilitate comparison with the reduced model. Supplementary Table 1 contains the full set of parameter values and their meaning. Figure 1 schematically illustrates the laser array (1).

Previous studies within the Lang-Kobayashi framework for a single laser have extensively reported on the dynamical routes to chaos, including stable locking, switching dynamics (particularly in short-cavity regimes[57,58]) and periodic oscillations[59,60]. However, these studies have only documented switching dynamics rather than the distinct single-pulse or multi-pulse operation reported in this work (see the Supplementary Material for possible single-laser non-pulsing dynamics). We will also emphasize that pulsing conditions are encountered for moderate-to-strong feedback strengths and bias currents high above the lasing threshold. The latter differs from most of the pulsing schemes mentioned above, which require the laser to be biased close to the threshold to optimize the pulse characteristics.

Numerical simulations.

For a large array of 30 semiconductor lasers, intensity time traces of pulsing are shown in Fig. 2. Several conditions of operation are highlighted to prove the tunability of the pulsing pattern, with a single pulse per period in Fig. 2 (b), two pulses per period in Fig. 2 (c), three pulses per period in Fig. 2 (d), and four pulses per period in Fig. 2 (e), with the peculiarity, in the latter, that the time interval between each pulse differs inside a train of pulses. The periodicity of pulses and pulse trains is very close to the external cavity time delay τ. There can be up to three characteristic time scales (one for cavity round-trip time, one for intervals between pulse trains, and one for intervals between the pulses within a single pulse train) at stake in this nonlinear phenomenon. Figure 2 shows two distinct pulsing dynamics within the array, with even-numbered lasers exhibiting one pattern and odd-numbered lasers displaying another pattern. This stems from the choice of frequency detuning set with ω_q in (1) presented in this study ($f_q=\omega_q/2\pi=2$ GHz for even-numbered lasers and $f_q=-2$ GHz for odd-numbered lasers). This choice of detuning helps illustrate the pulsing mechanism but does not contrast strongly with other detuning configurations detailed in the Supplementary Material. This detuning configuration was engineered to better enable pulsing, although other non-alternating detuning configurations can also induce pulsing. While one might expect the pulse count dependence shown in Fig. 2 (a) to exhibit a devil's staircase structure - akin to frequency locking observed in modulated external-cavity semiconductor lasers[61], fiber lasers[62], and frequency comb lasers[63] - the presence of multiple plateaus is more likely a result of multistability among coexisting states in the large, 30-laser array. As we show in the following subsection, the devil's staircase behavior becomes more pronounced in the simpler two-laser configuration.

Figure 3 provides a more detailed view of the overall behavior of the 30-laser array. In the single-pulse case, as shown in Fig. 3 (a), the lasers exhibit alternating dynamics: even-numbered lasers follow a similar pulsing pattern, while odd-numbered lasers share a distinct yet comparable behavior. The only notable deviation occurs at the edges of the array, where the network interactions are slightly different, resulting in less pronounced pulsing. Figure 3 (b) details the evolution of coherence over time, displaying the combined field intensity (black curve) and the Kuramoto order parameter in the inset (blue curve). The combined field intensity is given by: $\mathscr{C}(t)=|\sum_{q=1}^{Q}E_q(t)|^2$. This metric complements the complex Kuramoto order parameter[64,65], which is defined as $R(t)e^{i\Phi(t)}=\frac{1}{Q}\sum_{q=1}^{Q}\exp(i\phi_q(t))$ and reaches 1 when all lasers are in-phase synchronized and 0 when they are anti-phase synchronized. For comparison, the green curve represents the intensity of one of the even lasers, scaled by 30^2, while the orange curve shows the intensity of one of the odd lasers, similarly scaled. A notable feature is the pronounced dip in the combined field intensity, which occurs when the even-numbered lasers pulse. At the dip's lowest point, the lasers are anti-phase

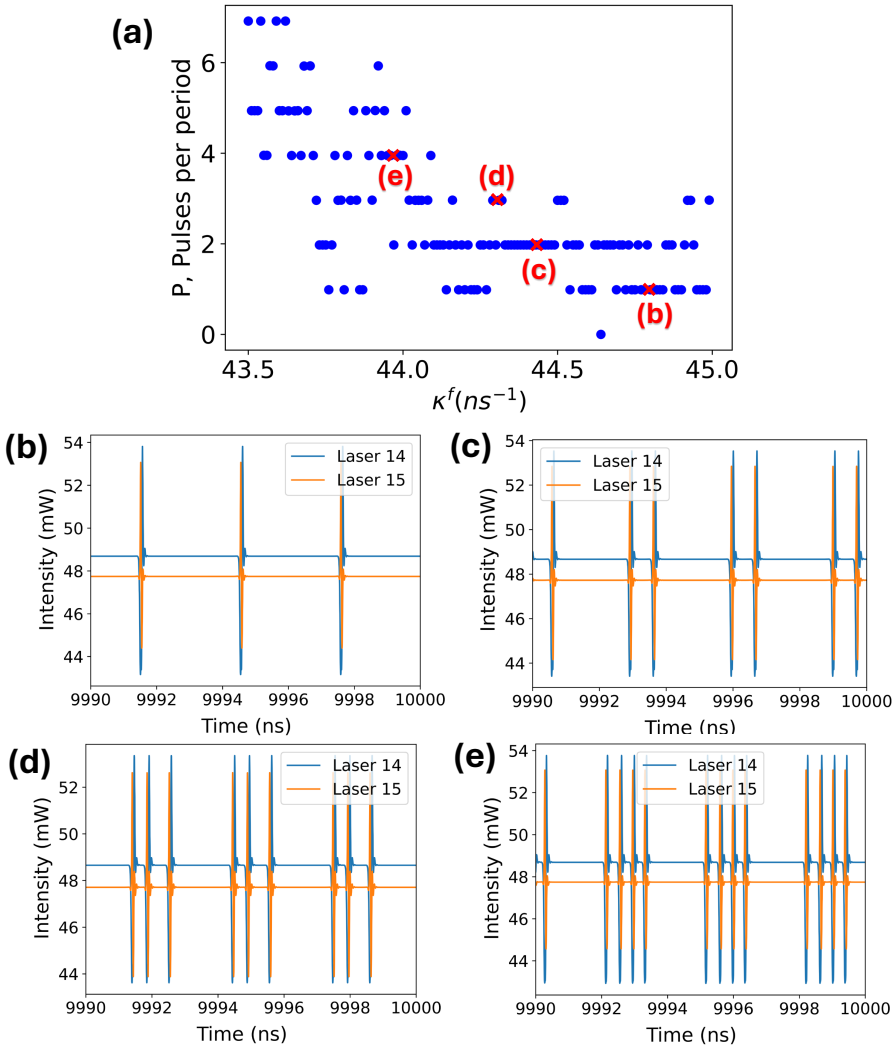

Figure 2. Multi-pulse dynamics in a 30-laser array under varying feedback strength. (a) Number of pulses per period as a function of feedback strength κ^f, obtained from a parameter sweep of the 30-laser system (1) after transient dynamics have been discarded. As κ^f varies, the number of pulses per period switches between discrete values, indicating multistability. The same set of randomly chosen initial conditions is used for all simulations. (b)–(e) Time traces of representative lasers showing distinct pulsing regimes at different values of κ^f: (b) single pulse per period for $\kappa^f = 44.8ns^{-1}$; (c) two pulses per period for $\kappa^f = 44.4ns^{-1}$; (d) three pulses per period for $\kappa^f = 44.31ns^{-1}$; (e) four pulses per period for $\kappa^f = 43.99ns^{-1}$. In each panel (b)-(e), the blue trace corresponds to laser #14, representative of the even-numbered lasers, while the orange trace shows laser #15, representative of the odd-numbered group.

synchronized. A few tens of picoseconds later, the odd-numbered lasers pulse in phase with the Kuramoto order parameter approaching 1. This alternating pattern between even- and odd-numbered lasers persists when the system is configured for two pulses per period, as seen in Fig. 3 (c)-(d), with a strong dip triggered when the even lasers are pulsing. In all other multi-pulsing cases, the pattern remains consistent (not shown). The number of dips in the combined field intensity matches the number of pulses per period, and the Kuramoto order parameter remains high (above 96%) when the odd-numbered lasers are pulsing. Notably, very similar pulsing dynamics are persistent when random perturbations are added to the frequency-detuning values. Supplementary Table 2 gives an example of perturbed detunings that preserve pulsing similar to what is shown in Fig. 3 (see Supplementary Fig. 2). Similar pulse dynamics also robustly appear in a 20-laser array with a sparse frequency detuning configuration (Supplementary Fig. 3). Unlike other laser networks, particularly those using saturable absorbers[15], pulsing in our array occurs simultaneously across all lasers without spatial propagation over time. This results in high-phase synchrony during the pulsing state, which is advantageous for beam combining. Achieving nearly perfect coherence is particularly relevant in large laser arrays, as optical power scales with the square of the number of emitters along the propagation axis.

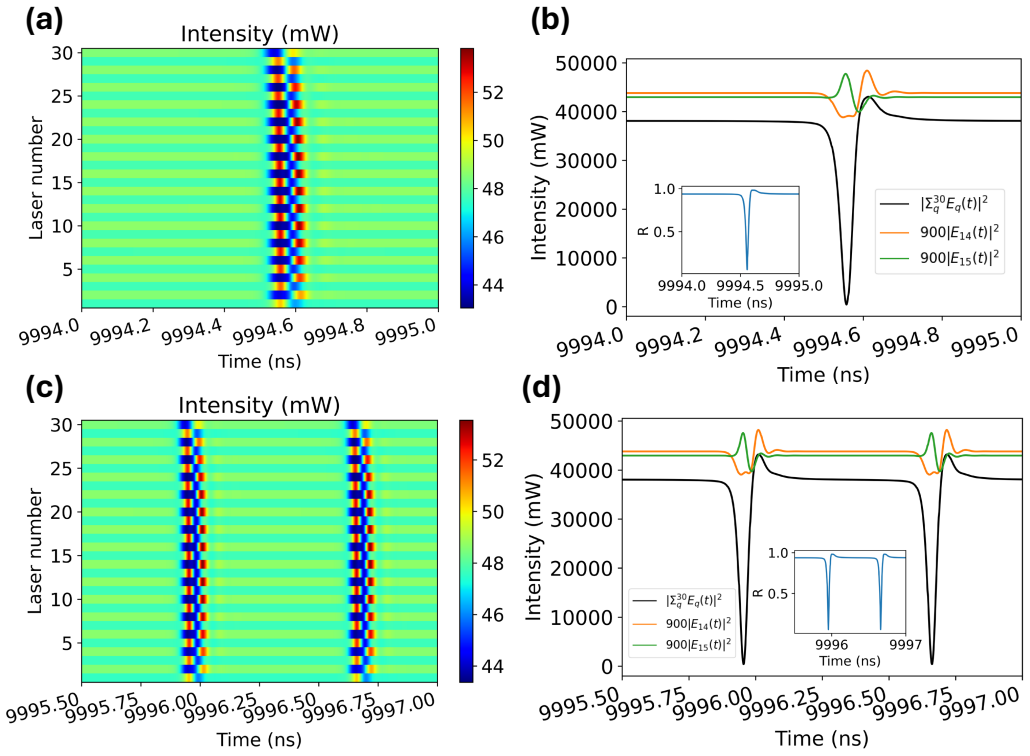

Figure 3. (a) Heatmap of single-pulse dynamics in a 30-laser array with distinct behaviors between odd- and even-numbered lasers. (b) Combined field intensity (black curve) of the 30 lasers, highlighting anti-phase and in-phase synchronization periods. The panel also shows the magnified intensity of an odd laser (green curve) and an even laser (orange curve). The inset demonstrates the Kuramoto order parameter $R(t)$, confirming transitions between anti-phase and in-phase synchrony. The feedback strength $\kappa^f = 44.8ns^{-1}$. (c-d) Same as (a)-(b) but for a pattern with two pulses per period, $\kappa^f = 44.4ns^{-1}$.

Mechanism for pulse generation.

To isolate the fundamental mechanisms of pulsing without the complexity of larger arrays, we consider the minimal laser array (1) with $Q = 2$ and $A_{qj} = 1$. This system can be expressed in polar coordinates for the laser field $E_q(t)$ as:

$$\begin{aligned}
\dot{r}_q &= Gr_q(t) + \tfrac{\kappa^f}{2}\sum_{j=1}^{2} r_j(t-\tau)\cos\left(\phi_j(t-\tau)-\phi_q(t)\right), \\
\dot{\phi}_q &= \alpha G + \omega_q + \tfrac{\kappa^f}{2}\sum_{j=1}^{2} \tfrac{r_j(t-\tau)}{r_q(t)}\sin\left(\phi_j(t-\tau)-\phi_q(t)\right), \\
\dot{N}_q &= \beta J_{th} - \gamma_n N_q - \left(2G(r_q,N_q)+\gamma\right) r_q^2,\ q = 1,2,
\end{aligned} \tag{2}$$

where function $G = \frac{1}{2}\left(g\frac{N_q(t)-N_0}{1+sr_q^2(t)} - \gamma\right)$, $r_q(t)$, and $\phi_q(t)$ are the complex field magnitude and phase, respectively. We aim to derive an analytically tractable model that captures how rapid, periodic phase destabilization and pulsing period oscillations, driven by frequency detuning, lead to the emergence of single- and multi-pulse dynamics. Simulations of the array (2), as shown in Supplementary Fig. 4, suggest two key approximations near the coherent pulsing state: (i) the pulsing period is close to the time-delay τ, implying that phase differences $\eta_1(t) = \phi_1(t-\tau) - \phi_1(t)$ and $\eta_2(t) = \phi_1(t-\tau) - \phi_1(t)$ are small; and (ii) $r_1(t)$ and $N_1(t)$ are close to $r_2(t)$ and $N_2(t)$, i.e., $r_1(t-\tau) \approx r_1(t) \approx r_2(t-\tau) \approx r_2(t) \equiv r(t)$ and $N_1(t-\tau) \approx N_1(t) \approx N_2(t-\tau) \approx N_2(t) \equiv N(t)$, where $r(t)$ and $N(t)$ correspond to a nearly coherent state. Further, our simulations indicate that variations in the pulsing periods of both lasers are approximately equal, i.e., we set $\eta_1(t) = \eta_2(t) = \eta(t)$. We then introduce the phase difference $\theta = \phi_1 - \phi_2$ whose evolution is governed by $\dot{\theta} = \Delta\omega + \frac{\kappa^f}{2}(\sin(\phi_2(t-\tau)-\phi_1(t)) - \sin(\phi_1(t-\tau)-\phi_2(t))$, where $\Delta\omega = \omega_1 - \omega_2$ is a frequency detuning. Similarly, the evolution of r is governed by $\dot{r} = Gr + \frac{\kappa^f}{2}r(t)(\cos(\phi_1(t-\tau)-\phi_1(t)) + \cos(\phi_2(t-\tau)-\phi_1(t))$. Applying the trigonometric identity for the difference of sines, we simplify the θ equation and obtain

the reduced system that approximately describes the collective dynamics close to the coherent state:

$$\begin{aligned}\dot{r} &= Gr + \tfrac{\kappa^f}{2}(\cos\eta(t) + \cos(\theta - \eta(t)))r(t),\\ \dot{\theta} &= \Delta\omega - \kappa^f \cos\eta(t)\sin\theta,\\ \dot{N} &= \beta J_{th} - \gamma N(t) - (2G+\gamma)\,r^2.\end{aligned} \tag{3}$$

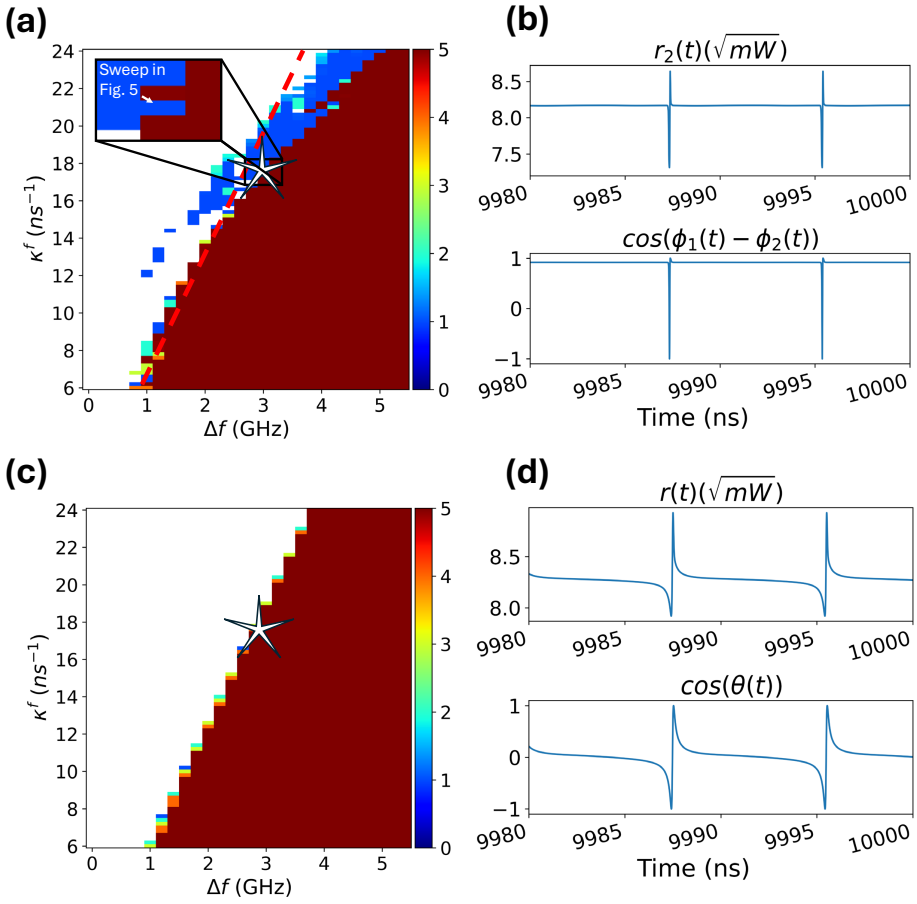

Figure 4. Pulse generation in the two-laser array (2) (a) and its reduced model (3) with $\eta = 0$ (c) as a function of the frequency detuning, $\Delta f = \Delta\omega/2\pi$, and feedback coupling strength, κ^f (in ns^{-1}). The color in the heatmaps (left panels, (a) and (c)) indicates the number of peaks per time period $T = \tau = 8$ ns. The blue region shows one-pulse dynamics, calculated over 100 trials in (a) to account for multistability and one trial in (c), all from random initial conditions. The white and dark red regions correspond to the lasers' steady operation and fast oscillatory behavior, respectively. The dark red color indicates five or more peaks per period. The red dashed curve in (a) represents the reduced model's saddle-node bifurcation curve $\kappa^f = \Delta f$ that adequately predicts the pulse generation boundary in (2). Note the gap on the x-axis highlighting the non-zero minimal frequency detuning required to induce pulsing at $\Delta f^* \approx 0.9$ GHz. The white star (left panels) and accompanying time traces (right panels, (b) and (d)) correspond to $\Delta f = 2.9192$ GHz and $\kappa^f = 17.5808$ ns^{-1}. Only the r_2 time series is plotted in (a), with nearly coherent $r_1(t)$ [not shown]. Parameters for these runs are shown in Supplementary Table 3. The inset in (a) highlights the region of the sweep the starred example comes from, and the arrow shows the location and direction of the parameter sweep featured in Fig. 5.

Note that the phase difference equation does not contain r and N and represents a variation of the non-autonomous Adler equation[66]. Its behavior is critically governed by the magnitude and evolution of pulsing period variation $\eta(t)$. In what follows, we show how the dynamics of η give rise to two distinct scenarios for generating either single or multi-pulse dynamics.

1. Single-pulse generation mechanism: $\eta = 0$.

Supplementary Figure 4 indicates that for single-pulse dynamics, $\eta \approx 0$, allowing us to simplify the θ equation in (3) to the classical non-uniform oscillator form[54]: $\dot{\theta} = \Delta\omega - \kappa^f \sin\theta$. This equation has two fixed points that disappear when $\Delta\omega$ exceeds κ^f. Under the condition that $\Delta\omega$ is slightly greater than κ^f, θ slowly drifts near a ghost state, emerging from a

saddle-node bifurcation at $\Delta\omega = k^f$, before rapidly completing the cycle. This rapid increase in the phase difference with θ reaching π destabilizes the r equation via the increased positive term $(1+\cos\theta)$ and induces a pulse in r. The time between the pulses is determined by the nonuniform oscillator's period[54]: $T_{period} = 2\pi/\sqrt{\Delta\omega^2 - (k^f)^2}$, where the denominator is small. Figure 4 shows that the reduced model (3) with $\eta = 0$ accurately predicts the onset of coherent single-pulse dynamics in the full Lang-Kobayashi model (2), induced by frequency heterogeneity through a saddle-node bifurcation on an invariant circle (SNIC)[54]. This mechanism is consistent with earlier analyses of the autonomous, time-delayed Adler equation and has been linked phenomenologically to pulsing in laser arrays[51–53]. However, unlike prior works, our derivation connects this mechanism explicitly to the Lang-Kobayashi model via the reduced system (3). Nevertheless, as with its autonomous Adler counterpart, the simplified, reduced model (3) with $\eta = 0$ has a fundamental limitation: it cannot account for multi-pulse dynamics. Capturing such behavior requires retaining the time-dependent nature of $\eta(t)$, allowing the pulsing period to oscillate. From a historical perspective, we first derived the reduced model (3), which suggested that small, persistent oscillations in η could introduce a second emergent frequency governing the number and spacing of multiple pulses per cycle. This insight was then validated through simulations of the full model (2), leading to the following understanding.

2. Multi-pulse generation mechanism: the role of oscillating pulsing periods

Figure 5 illustrates the emergence of multi-pulse dynamics in the full model (2), focusing on the parameter region highlighted in the inset of Fig. 4. By varying the feedback strength κ^f and the frequency detuning magnitude in a way that keeps the system near the saddle-node bifurcation transition from single- to multi-pulse regimes, we observe a dependence of the pulse number p that resembles a devil's staircase (Fig. 5 (a)). Unlike the more fragmented dependence seen in the 30-laser array (Fig. 2), the two-laser system (2) exhibits a classical, well-defined staircase structure. Remarkably, Figs. 5(b)-(d) reveal predicted oscillating behavior in $\eta_2 = \phi_2(t-\tau) - \phi_2(t)$ which governs the number of generated pulses per period. This oscillatory behavior is evident in the periodic repetition of the local maxima of η_2.

Figure 6 presents simulations of the reduced model (3) where $\eta(t)$ is taken from the full model (2). These results confirm that the reduced model successfully captures the emergence and structure of multi-pulse dynamics observed in the full Lang-Kobayashi system (2). Moreover, it sheds light on the underlying mechanism of multi-pulse generation, which rests on two key features: (i) the θ equation of reduced system (3) undergoes a saddle-node bifurcation at fixed values of $\eta^* = \pm\arccos(\Delta\omega/\kappa^f)$; and (ii) the oscillating behavior of $\eta(t)$ enables the phase θ to make multiple 2π rotations during intervals where $|\eta(t)| > |\eta^*|$, i.e., when $\dot{\theta} > 0$. The number of such rotations per cycle determines the number of pulses p. During the remaining portion of the cycle where $|\eta(t)| < |\eta^*|$, the phase θ remains at a stable fixed point corresponding to a quiescent (non-pulsing) phase.

To illustrate the multi-pulse generation mechanism more transparently, we introduce a phenomenological model in the form of a non-autonomous Adler equation[66], which captures the behavior of the reduced model's phase dynamics and simplifies analytical treatment. The model takes the form:

$$\frac{d\theta}{dt} = \Delta\omega - \kappa^f(1 + a\cos\Omega t)\sin\theta, \tag{4}$$

where Ω represents the emerging angular frequency associated with the oscillations in $\eta(t)$ and a is a scaling factor modulating the amplitude of the periodic forcing. The analysis of this phenomenological model (4), detailed in the Methods section, yields an explicit expression for the number of pulses per modulation cycle as a function of the system parameters:

$$p = F(a, \Omega, \Delta\omega, k^f) \tag{5}$$

with the right-hand side function given via (12)-(13) (see Methods). As shown in Fig. 7, the analytical prediction for p closely matches the results from the direct simulations of the phenomenological model (4), further validating the proposed multi-pulse mechanism.

Discussion

While single pulsing in diode lasers is a well-established phenomenon, it typically requires additional mechanisms, such as external current modulation or saturable absorbers, to induce pulsation. In contrast, the multi-pulsing dynamics we uncovered arise naturally from engineered frequency detuning and appropriate selection of diode and external cavity parameters, without any active modulation. Building on this foundation, we addressed a long-standing challenge in photonics, namely the realization of synchronized multi-pulse generation in large semiconductor laser arrays—a key bottleneck in scaling high-power pulsed optical systems. We show that direct-current-driven external-cavity arrays, subject only to optical feedback and non-local time-delayed coupling, can robustly produce periodic, coherent, high-power pulse trains, including complex multi-pulse structures. Rather than relying on external forcing, this behavior emerges intrinsically through engineered heterogeneity in intrinsic laser frequencies, offering a powerful and experimentally accessible design principle for achieving scalable and highly controllable multi-pulsing in integrated photonic platforms.

We uncovered the underlying mechanism within the Lang-Kobayashi laser framework, showing that certain, potentially wide, distributions of intrinsic laser frequencies give rise to a two-cluster coherent state that supports both single- and multi-pulse regimes. The transition to multi-pulsing is driven by heterogeneity-induced interburst oscillations. These dynamics are captured by a reduced model explicitly linked to the Lang-Kobayashi equations and further clarified through a phenomenological, analytically tractable version resembling a non-autonomous Adler equation. Together, these models reveal that the number of pulses per burst is accurately determined by the emergent interburst frequency. Importantly, the period of coherent pulsing closely follows the external cavity round-trip time, with subtle, time-varying deviations. These deviations align with the phase difference between the two laser clusters, as supported by Supplementary Fig. 5. This observation highlights a crucial role for frequency heterogeneity, both between and within clusters, in shaping the phase dynamics that ultimately determine the number of pulses in each cycle.

Our analysis assumes an identical feedback phase across the array, i.e., no feedback misalignment, which allows for the derivation of a consistent analytical framework that bridges the Lang-Kobayashi and Adler models. However, our findings are not limited to this idealized setting. Simulations incorporating delay-time perturbations (e.g., standard deviations of 20 ps) show that coherent pulsing persists even when the feedback phase varies randomly between lasers. This robustness suggests that phase alignment is not a strict requirement for realizing coherent, controllable pulsing in large arrays. Remarkably, we demonstrate that pulse characteristics are strongly dependent on the detuning pattern across the array. This suggests that coherent pulse generation can be experimentally controlled via methods such as individual bias current tuning and other means.

Very recently, coherent picosecond bright solitons were experimentally demonstrated on a DC-driven mid-infrared quantum cascade laser chip[67]. In that work, laser pulses emerge from a fast bistable nonlinear resonator, eliminating the need for external modulation or saturable absorbers[68] — a significant milestone toward realizing a miniature, integrated photonic chip that emits very narrow, high-frequency pulses. While the specific laser architecture, pulse generation mechanisms, and pulsation patterns may differ—particularly in the recent demonstration, which focuses on single-pulse emission—the generation of narrow, high-frequency, high-power, periodic, and controllable multi-pulse trains in DC-driven external-cavity diode laser arrays in our model also makes it a promising candidate for compact photonic designs targeting diode lasers governed by relaxation oscillation limits. This self-organized, periodic pulse formation arises solely from direct current drive and time-delayed optical feedback, with a notable distinction in our setting: the emergence of coherent multi-pulse dynamics across large laser arrays. These recent experimental advances[67] support the broader relevance of our theoretical findings and underscore the growing convergence between active and passive nonlinear photonic systems. Our findings pave the way for practical applications, including high-power pulsed beam combining and neuromorphic photonic computing. More broadly, the multi-pulse generation mechanism we described may apply to a range of excitable physical and biological systems where coherent burst dynamics are shaped by structural heterogeneity and delayed interactions.

Methods

Analysis of the phenomenological model

The dynamics of the phenomenological model (4) can be analyzed using a slow-fast decomposition. Rewriting the model in rescaled time $t_{new} = \kappa^f t$, we obtain

$$\begin{aligned} \frac{d\theta}{dt_{new}} &= \nu - (1 + a\cos\psi)\sin\theta, \\ \frac{d\psi}{dt_{new}} &= \mu, \end{aligned} \tag{6}$$

where $\nu = \frac{\Delta\omega}{\kappa^f}$, $\frac{\Omega}{\kappa^f} = \mu$, and the auxiliary variable $\psi = \Omega t$ captures the phase of the time-varying modulation. In this formulation, θ is the fast variable, and ψ evolves slowly when $\mu \ll 1$, enabling the use of singular perturbation techniques to analyze the system. We treat ψ as a slowly varying parameter in the fast subsystem, which provides a sequence of phase portraits that govern the overall system dynamics and shape the emergence of multi-pulsing behavior.

1. Fast subsystem. Setting $\mu = 0$, we obtain the fast system:

$$\begin{aligned} \frac{d\theta}{dt_{new}} &= \nu - (1 + a\cos\psi)\sin\theta, \\ \psi &= C, \end{aligned} \tag{7}$$

where C is a constant. This system mimics the reduced model (3) with constant η and, as such, supports only single-pulse generation via a SNIC bifurcation.

Case I. When $\cos\psi < \frac{\nu-1}{a}$, the system (7) has no fixed points and undergoes continuous phase rotation with the period

$$T(\psi) = \frac{2\pi}{\sqrt{\nu^2 - (1 + a\cos\psi)^2}}. \tag{8}$$

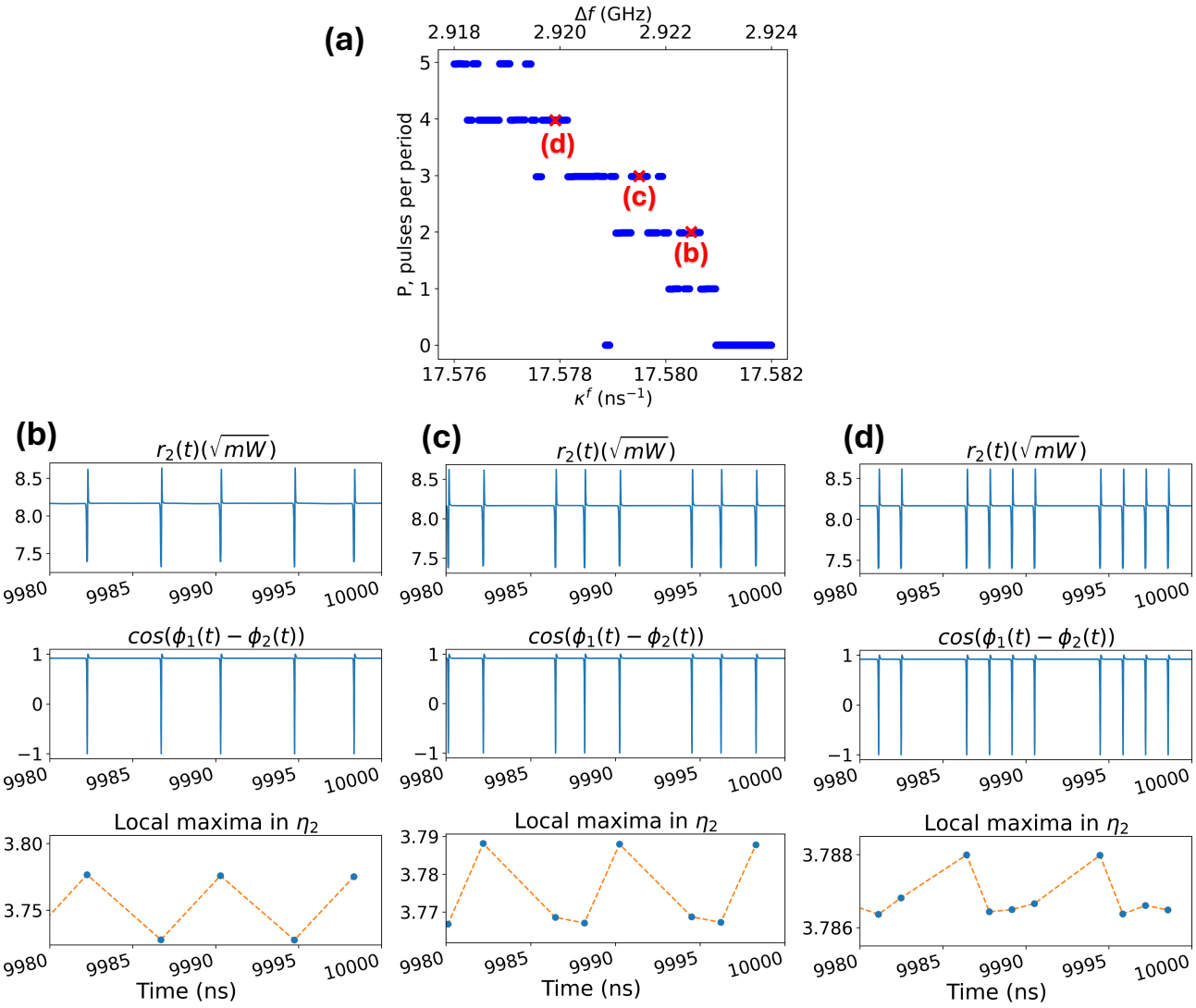

Figure 5. Multi-pulse dynamics in the two-laser model (2). (a) Number of pulses per period obtained from a parameter sweep, where the feedback strength κ^f is increased while the frequency detuning Δf is decreased by the same numerical value, following the dependence shown in the inset in Fig. 4. (b)–(d) Time traces of $r_2(t)$ and $cos(\phi_1(t) - \phi_2(t))$, along with the peak values $\eta_2 = \phi_2(t-\tau) - \phi_2(t)$, for representative cases exhibiting increasing numbers of pulses per period: (b) two pulses per period: $\kappa^f = 17.5805$ ns^{-1} and $\Delta f = 2.9195$ GHz; (c) three pulses per period: $\kappa^f = 17.5795$ ns^{-1} and $\Delta f = 2.9205$ GHz; (d) four pulses per period: $\kappa^f = 17.5779$ ns^{-1} and $\Delta f = 2.9221$ GHz. In all cases, oscillations in η_2 exhibit periodic behavior with a period close to τ. Similar behavior is observed in $\eta_1 = \phi_1(t-\tau) - \phi_1(t)$ [not shown].

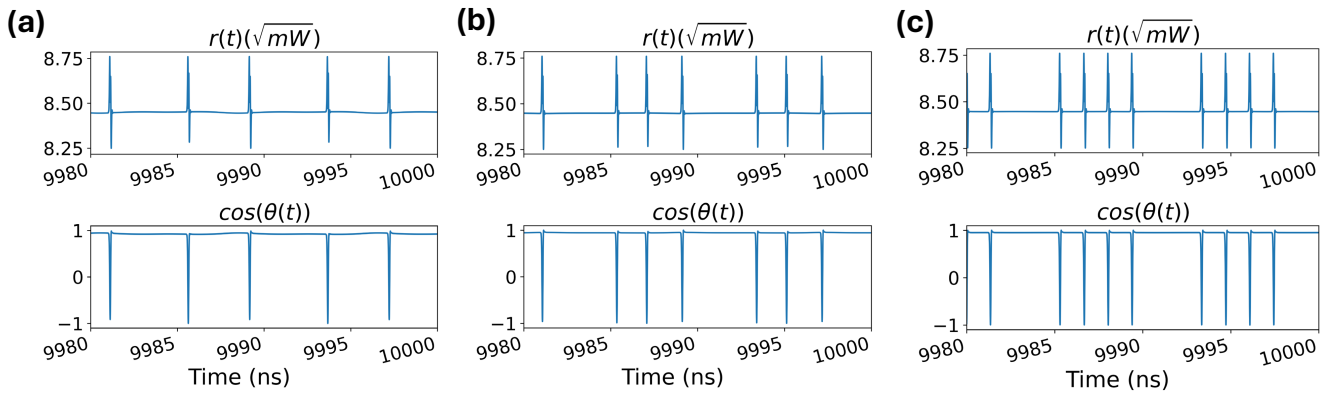

Figure 6. Multi-pulse dynamics in the reduced model. Time traces of $r(t)$ and $\cos\theta$, calculated from the reduced model (3) with time-dependent $\eta(t) \equiv \eta_1 = \phi_1(t-\tau) - \phi_1(t)$, where $\eta(t)$ is taken from the full model. (a)-(c) Simulations correspond to the two-, three-, and four-pulsing regimes observed in Fig. 5 (b)-(d), using the same values of κ^f and Δf. (a) Two pulses per period: $\kappa^f = 17.5805$ ns $^{-1}$, $\Delta f = 2.9195$ GHz; (b) three pulses per period: $\kappa^f = 17.5795$ ns $^{-1}$, $\Delta f = 2.9205$ GHz; (c) four pulses per period: $\kappa^f = 17.5779$ ns $^{-1}$, $\Delta f = 2.9221$ GHz. The reduced model predicts the pulsing dynamics of the full system with high accuracy, capturing both pulse multiplicity and timing.

The interval of the system's phase rotation is

$$I_{rot} = \{\psi_0 < \psi < 2\pi - \psi_0\}, \quad \text{where} \quad \psi_0 = \arccos\left(\frac{\nu-1}{a}\right). \tag{9}$$

Case II. When $\cos\psi > \frac{\nu-1}{a}$, the system (7) has a stable fixed point $\theta^* = \arcsin(\frac{\nu}{1+a\cos\psi})$ and phase rotation ceases. The fixed-point regime occurs within the interval $I_{fp} = \{-\psi_0 < \psi < \psi_0\}$.

2. Full system dynamics. For $\mu > 0$, ψ evolves slowly, and the full system (6) alternates between rotational (Case I) and fixed-point (Case II) dynamics. The duration spent in the rotation interval I_{rot} is:

$$T_{rot} = (2\pi - 2\psi_0)/\mu. \tag{10}$$

During this interval, the phase θ can make full 2π rotations. The number of such rotations determines the number of pulses p within the rotation interval I_{rot}. The average period of the rotation time that yields one pulse can be estimated as:

$$T_{pulse} = \frac{1}{2\pi - 2\psi_0} \int_{\psi_0}^{2\pi-\psi_0} T(\psi)\, d\psi, \tag{11}$$

with $T(\psi)$ and ψ_0 are given in (8) and (10), respectively. Therefore, the average number of pulses can be calculated as:

$$p = \frac{T_{rot}}{T_{pulse}} = \frac{(2\pi - 2\psi_0)^2}{\mu \int_{\psi_0}^{2\pi-\psi_0} T(\psi)\, d\psi} = \frac{(2\pi - 2\psi_0)^2}{\mu \int_{\psi_0}^{2\pi-\psi_0} \frac{2\pi}{\sqrt{\nu^2 - (1+a\cos\psi)^2}}\, d\psi}, \tag{12}$$

where the integral in the denominator can be calculated symbolically as:

$$\int \frac{2\pi}{\sqrt{\nu^2 - (1+a\cos(\psi))^2}} d\psi = \frac{32\pi\cos^2\left(\frac{\psi}{2}\right)\sqrt{\frac{a\cos(\psi)-\nu+1}{(a-\nu+1)(\cos(\psi)+1)}}\sqrt{\frac{a\cos(\psi)+\nu+1}{(a+\nu+1)(\cos(\psi)+1)}}\sqrt{\frac{-a^2\cos^2(\psi)-2a\cos(\psi)+\nu^2-1}{(\cos(\psi)+1)^2}}\,\mathscr{F}}{\sqrt{\frac{a-\nu-1}{a+\nu+1}}\sqrt{a^2(-\cos(2\psi))-a^2-4a\cos(\psi)+2\nu^2-2}\sqrt{-\sec^4\left(\frac{\psi}{2}\right)\left(a^2\cos(2\psi)+a^2+4a\cos(\psi)-2\nu^2+2\right)}}, \tag{13}$$

with $\mathscr{F} = F\left(\sin^{-1}\left(\sqrt{\frac{a-\nu-1}{a+\nu+1}}\tan\left(\frac{\psi}{2}\right)\right)\middle|\frac{(a+\nu-1)(a+\nu+1)}{a^2-2\nu a+\nu^2-1}\right)$, where $F(x|m)$ is the elliptic integral of the first kind. By rescaling the parameters in (12)-(13) back to the original parameters in the phenomenological model (4) and taking the integer part to ensure $p \in \mathbb{Z}$, we arrive at the general formula (5) for predicting the number of pulses per cycle. This formula is used to generate the analytical estimate shown in Fig. 7 (a).

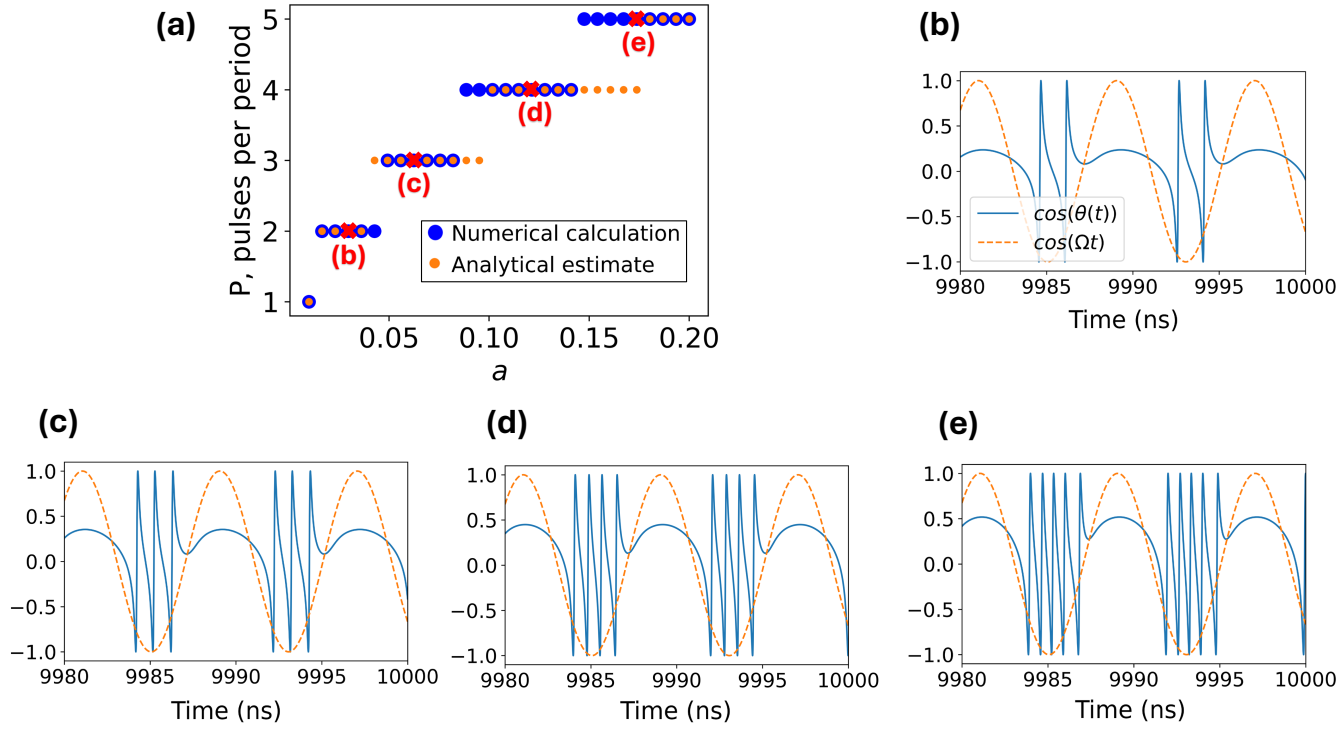

Figure 7. Multi-pulse generation in the phenomenological model. (a) Number of pulses per period as a function of the modulation amplitude a, computed from direct numerical simulations of the phenomenological model (4) (blue dots) and from the analytical prediction based on Eqs. (12)-(13), with only the integer part p shown (orange dots). (b)-(e) Time traces $\theta(t)$ (blue) and $\cos(\Omega t)$ (orange) for representative cases with increasing numbers of pulses per period: (b) two pulses per period, $a = 0.03$, (c) three pulses per period, $a = 0.07$, (d) four pulses per period, $a = 0.12$, (e) five pulses per period, $a = 0.017$. $\Omega = 0.785$ corresponds to the time period of η in the reduced model in Fig. 6 (a). $\kappa^f = 17.52\ \mathrm{ns}^{-1}$.

Data availability

All relevant data are available from the authors upon reasonable request.

Code availability

Matlab or Python code is also available from the authors upon reasonable request.

References

1. Prucnal, P. R., Shastri, B. J., Ferreira de Lima, T., Nahmias, M. A. & Tait, A. N. Recent progress in semiconductor excitable lasers for photonic spike processing. *Adv. Opt. Photonics* **8**, 228–299 (2016).
2. Robertson, J., Wade, E., Kopp, Y., Bueno, J. & Hurtado, A. Toward neuromorphic photonic networks of ultrafast spiking laser neurons. *IEEE J. Sel. Top. Quantum Electron.* **26**, 7700715 (2020).
3. Nakajima, M., Tanaka, K. & Hashimoto, T. Scalable reservoir computing on coherent linear photonic processor. *Commun. Phys.* **4**, 20 (2021).
4. Zbik, M. Sub-nanosecond pulsed quantum cascade laser driver. In *CLEO: Applications and Technology*, AF3K–7 (Optica Publishing Group, 2019).
5. Chen, Y., Winful, H. & Liu, J. Subharmonic bifurcations and irregular pulsing behavior of modulated semiconductor lasers. *Appl. Phys. Lett.* **47**, 208–210 (1985).
6. Hemery, E., Chusseau, L. & Lourtioz, J.-M. Dynamic behaviors of semiconductor lasers under strong sinusoidal current modulation: modeling and experiments at 1.3 mu m. *IEEE J. Quantum Electron.* **26**, 633–641 (1990).
7. Tredicce, J. R., Arecchi, F. T., Lippi, G. L. & Puccioni, G. P. Instabilities in lasers with an injected signal. *JOSA B* **2**, 173–183 (1985).
8. Wieczorek, S., Krauskopf, B. & Lenstra, D. Multipulse excitability in a semiconductor laser with optical injection. *Phys. Rev. Lett.* **88**, 063901 (2002).
9. Goulding, D. *et al.* Excitability in a quantum dot semiconductor laser with optical injection. *Phys. Rev. Lett.* **98**, 153903 (2007).
10. Downey, P., Bowers, J., Tucker, R. & Agyekum, E. Picosecond dynamics of a gain-switched InGaAsP laser. *IEEE J. Quantum Electron.* **23**, 1039–1047 (1987).
11. Liu, H.-F., Fukazawa, M., Kawai, Y. & Kamiya, T. Gain-switched picosecond pulse ($\leq$ 10 ps) generation from 1.3 μm InGaAsP laser diodes. *IEEE J. Quantum Electron.* **25**, 1417–1425 (1989).
12. Haus, H. A theory of forced mode locking. *IEEE J. Quantum Electron.* **11**, 323–330 (1975).
13. Liu, X. & Cui, Y. Revealing the behavior of soliton buildup in a mode-locked laser. *Adv. Photonics* **1**, 016003–016003 (2019).
14. Haus, H. A. Theory of mode locking with a fast saturable absorber. *J. Appl. Phys.* **46**, 3049–3058 (1975).
15. Puzyrev, D., Vladimirov, A., Pimenov, A., Gurevich, S. & Yanchuk, S. Bound pulse trains in arrays of coupled spatially extended dynamical systems. *Phys. Rev. Lett.* **119**, 163901 (2017).
16. Perego, A. & Lamperti, M. Collective excitability, synchronization, and array-enhanced coherence resonance in a population of lasers with a saturable absorber. *Phys. Rev. A* **94**, 033839 (2016).
17. Alfaro-Bittner, K., Barbay, S. & Clerc, M. Pulse propagation in a 1D array of excitable semiconductor lasers. *Chaos: An Interdiscip. J. Nonlinear Sci.* **30**, 083136 (2020).
18. Spitz, O., Maldonado-Castillo, L. E., Berrill, M. A. & Braiman, Y. Optimization of combined coherent gain-switch pulsing in a large array of semiconductor lasers. *IEEE J. Sel. Top. Quantum Electron.* **31**, 1501614 (2025).
19. Münkel, M., Kaiser, F. & Hess, O. Spatio-temporal dynamics in semiconductor lasers with delayed optical feedback. *Int. J. Bifurc. Chaos* **8**, 951–963 (1998).
20. Scirè, A., Tessone, C. J. & Colet, P. Dynamics of coupled self-pulsating semiconductor lasers. *IEEE J. Quantum Electron.* **41**, 272–279 (2005).
21. Münkel, M., Kaiser, F. & Hess, O. Stabilization of spatiotemporally chaotic semiconductor laser arrays by means of delayed optical feedback. *Phys. Rev. E* **56**, 3868 (1997).

22. Otsuka, K. & Chern, J.-L. Synchronization, attractor fission, and attractor fusion in a globally coupled laser system. *Phys. Rev. A* **45**, 5052 (1992).

23. Winful, H. G. & Rahman, L. Synchronized chaos and spatiotemporal chaos in arrays of coupled lasers. *Phys. Rev. Lett.* **65**, 1575 (1990).

24. Sugawara, T., Tachikawa, M., Tsukamoto, T. & Shimizu, T. Observation of synchronization in laser chaos. *Phys. Rev. Lett.* **72**, 3502 (1994).

25. Roy, R. & Thornburg Jr, K. S. Experimental synchronization of chaotic lasers. *Phys. Rev. Lett.* **72**, 2009 (1994).

26. Kozyreff, G., Vladimirov, A. & Mandel, P. Dynamics of a semiconductor laser array with delayed global coupling. *Phys. Rev. E* **64**, 016613 (2001).

27. Masoller, C. Anticipation in the synchronization of chaotic semiconductor lasers with optical feedback. *Phys. Rev. Lett.* **86**, 2782 (2001).

28. Kouomou, Y. C., Colet, P., Gastaud, N. & Larger, L. Effect of parameter mismatch on the synchronization of chaotic semiconductor lasers with electro-optical feedback. *Phys. Rev. E* **69**, 056226 (2004).

29. Zamora-Munt, J., Masoller, C., Garcia-Ojalvo, J. & Roy, R. Crowd synchrony and quorum sensing in delay-coupled lasers. *Phys. Rev. Lett.* **105**, 264101 (2010).

30. Nixon, M. *et al.* Controlling synchronization in large laser networks. *Phys. Rev. Lett.* **108**, 214101 (2012).

31. Grillot, F., Gavrielides, A., Spitz, O., Newell, T. C. & Carras, M. Talbot coupling of an array of quantum cascade lasers. In *Quantum Sensing and Nano Electronics and Photonics XV*, vol. 10540, 224–231 (SPIE, 2018).

32. Ding, J., Belykh, I., Marandi, A. & Miri, M.-A. Dispersive versus dissipative coupling for frequency synchronization in lasers. *Phys. Rev. Appl.* **12**, 054039 (2019).

33. Honari-Latifpour, M., Ding, J., Belykh, I. & Miri, M.-A. Spectral principle for frequency synchronization in repulsive laser networks and beyond. *Chaos: An Interdiscip. J. Nonlinear Sci.* **35**, 021101 (2025).

34. Sheng, J., Wei, X., Yang, C. & Wu, H. Self-organized synchronization of phonon lasers. *Phys. Rev. Lett.* **124**, 053604 (2020).

35. Hillbrand, J. *et al.* In-phase and anti-phase synchronization in a laser frequency comb. *Phys. Rev. Lett.* **124**, 023901 (2020).

36. Khajavikhan, M., Hoyer-Leitzel, A. & Leger, J. R. Efficient conversion of light from sparse laser arrays into single-lobed far field using phase structures. *Opt. Lett.* **33**, 2377–2379 (2008).

37. Nyaupane, P. *et al.* Coherence and phase-locking in high-power, broad-area, highly heterogeneous blue diode laser arrays. *ACS Photonics* **12**, 597–609 (2025).

38. Braiman, Y., Lindner, J. F. & Ditto, W. L. Taming spatiotemporal chaos with disorder. *Nat.* **378**, 465–467 (1995).

39. Braiman, Y., Ditto, W., Wiesenfeld, K. & Spano, M. Disorder-enhanced synchronization. *Phys. Lett. A* **206**, 54–60 (1995).

40. Nishikawa, T. & Motter, A. E. Symmetric states requiring system asymmetry. *Phys. Rev. Lett.* **117**, 114101 (2016).

41. Belykh, I., Jeter, R. & Belykh, V. Foot force models of crowd dynamics on a wobbly bridge. *Sci. Adv.* **3**, e1701512 (2017).

42. Hart, J. D., Zhang, Y., Roy, R. & Motter, A. E. Topological control of synchronization patterns: Trading symmetry for stability. *Phys. Rev. Lett.* **122**, 058301 (2019).

43. Daley, K., Zhao, K. & Belykh, I. V. Synchronizability of directed networks: The power of non-existent ties. *Chaos: An Interdiscip. J. Nonlinear Sci.* **30**, 043102 (2020).

44. Zhang, Y., Ocampo-Espindola, J. L., Kiss, I. Z. & Motter, A. E. Random heterogeneity outperforms design in network synchronization. *Proc. Natl. Acad. Sci.* **118**, e2024299118 (2021).

45. Molnar, F., Nishikawa, T. & Motter, A. E. Asymmetry underlies stability in power grids. *Nat. Commun.* **12**, 1457 (2021).

46. Punetha, N. & Wetzel, L. Heterogeneity-induced synchronization in delay-coupled electronic oscillators. *Phys. Rev. E* **106**, L052201 (2022).

47. Eliezer, Y., Mahler, S., Friesem, A. A., Cao, H. & Davidson, N. Controlling nonlinear interaction in a many-mode laser by tuning disorder. *Phys. Rev. Lett.* **128**, 143901 (2022).

48. Liu, B., Liu, Y. & Braiman, Y. Coherent addition of high power laser diode array with a V-shape external Talbot cavity. *Opt. Express* **16**, 20935–20942 (2008).

49. Liu, B. & Braiman, Y. Coherent beam combining of high power broad-area laser diode array with near diffraction limited beam quality and high power conversion efficiency. *Opt. Express* **21**, 31218–31228 (2013).

50. Nair, N., Hu, K., Berrill, M., Wiesenfeld, K. & Braiman, Y. Using disorder to overcome disorder: A mechanism for frequency and phase synchronization of diode laser arrays. *Phys. Rev. Lett.* **127**, 173901 (2021).

51. Yanchuk, S., Ruschel, S., Sieber, J. & Wolfrum, M. Temporal dissipative solitons in time-delay feedback systems. *Phys. Rev. Lett.* **123**, 053901 (2019).

52. Munsberg, L., Javaloyes, J. & Gurevich, S. V. Topological localized states in the time delayed Adler model: Bifurcation analysis and interaction law. *Chaos: An Interdiscip. J. Nonlinear Sci.* **30**, 063137 (2020).

53. Garbin, B., Javaloyes, J., Tissoni, G. & Barland, S. Topological solitons as addressable phase bits in a driven laser. *Nat. Commun.* **6**, 5915 (2015).

54. Strogatz, S. H. *Nonlinear dynamics and chaos: with applications to physics, biology, chemistry, and engineering* (CRC press, 2018).

55. Chen, Z., Segev, M. & Christodoulides, D. N. Optical spatial solitons: historical overview and recent advances. *Reports on Prog. Phys.* **75**, 086401 (2012).

56. Lang, R. & Kobayashi, K. External optical feedback effects on semiconductor injection laser properties. *IEEE J. Quantum Electron.* **16**, 347–355 (1980).

57. Heil, T. *et al.* Delay dynamics of semiconductor lasers with short external cavities: Bifurcation scenarios and mechanisms. *Phys. Rev. E* **67**, 066214 (2003).

58. Tabaka, A., Panajotov, K., Veretennicoff, I. & Sciamanna, M. Bifurcation study of regular pulse packages in laser diodes subject to optical feedback. *Phys. Rev. E* **70**, 036211 (2004).

59. Masoller, C. Spatiotemporal dynamics in the coherence collapsed regime of semiconductor lasers with optical feedback. *Chaos: An Interdiscip. J. Nonlinear Sci.* **7**, 455–462 (1997).

60. Dong, J.-X., Ruan, J., Zhang, L., Zhuang, J.-P. & Chan, S.-C. Stable-unstable switching dynamics in semiconductor lasers with external cavities. *Phys. Rev. A* **103**, 053524 (2021).

61. Baums, D., Elsässer, W. & Göbel, E. O. Farey tree and devil's staircase of a modulated external-cavity semiconductor laser. *Phys. Rev. Lett.* **63**, 155 (1989).

62. Wu, X. *et al.* Farey tree and devil's staircase of frequency-locked breathers in ultrafast lasers. *Nat. Commun.* **13**, 5784 (2022).

63. Liu, G. *et al.* Farey tree locking of terahertz quantum cascade laser frequency combs. *Light. Sci. & Appl.* **14**, 147 (2025).

64. Acebrón, J. A., Bonilla, L. L., Pérez Vicente, C. J., Ritort, F. & Spigler, R. The Kuramoto model: A simple paradigm for synchronization phenomena. *Rev. Mod. Phys.* **77**, 137–185 (2005).

65. Kazakov, D. *et al.* Cluster synchronization in a semiconductor laser. *APL Photonics* **9**, 026104 (2024).

66. Gandhi, P., Knobloch, E. & Beaume, C. Dynamics of phase slips in systems with time-periodic modulation. *Phys. Rev. E* **92**, 062914 (2015).

67. Kazakov, D. *et al.* Driven bright solitons on a mid-infrared laser chip. *Nat.* **642**, 1–7 (2025).

68. Genevet, P., Barland, S., Giudici, M. & Tredicce, J. R. Stationary localized structures and pulsing structures in a cavity soliton laser. *Phys. Rev. A* **79**, 033819 (2009).

Acknowledgements

This work is supported by the Office of Naval Research. The authors thank Vladimir Belykh for his invaluable input, Mark A. Berrill for his help in developing optimized numerical tools for the time-delayed system simulations, and Matthew Crespo for his initial work on the topic of pulsing laser arrays.

Author contributions statement

Conceptualization: O.S., Y.B. Methodology: O.S., A.M., I.B., Y.B. Investigation: G.S., K.G., I.B., A.M. Visualization: G.S., K.G., A.M. Supervision: O.S., I.B., Y.B. Writing – original draft: G.S., O.S., I.B., Y.B. Writing – review and editing: G.S., K.G., O.S., A.M., I.B., Y.B.

Competing interests

The authors declare no competing interests.

Supplementary information: Coherent multi-pulsing induced by engineered heterogeneity in diode laser arrays

Greggory Scranton[1], Kendall Golden[2], Olivier Spitz[1,*], Arindam Mishra[1], Igor Belykh[2,†], and Yehuda Braiman[1,3,‡]

[1]The College of Optics and Photonics (CREOL), University of Central Florida, Orlando, FL 32816, USA
[2]Department of Mathematics and Statistics and Neuroscience Institute, Georgia State University, P.O. Box 4110, Atlanta, Georgia, 30302-410, USA
[3]Department of Electrical and Computer Engineering, University of Central Florida, Orlando, FL 32816, USA
[*]olivier.spitz@ucf.edu
[†]ibelykh@gsu.edu
[‡]yehuda.braiman@ucf.edu

Single-laser dynamics with the Lang-Kobayashi models

The peculiarity of pulsing within the framework of this study is that it requires a network of emitters to be triggered. This process can be optimized with adequate engineered frequency detuning, as highlighted in the main text. Yet, our model can also be studied in the context of a single laser subject to external optical feedback, and in this case, it does not show pulsing dynamics. Details about the nonlinear dynamics that can be observed in this configuration are found in Supplementary Fig. 1, and those states are in good agreement with prior studies about the same configuration.[1,2] It is relevant to note that, in the case of an array of lasers, the same dynamics can also be observed, but we only focused on the pulsing state as it has not been reported previously. For a high bias current (seven times) above the threshold, Supplementary Fig. 1 (a) shows that the single laser exhibits a steady-state behavior up to an intermediate feedback level of 10 ns^{-1}. The corresponding unwrapped phase in Supplementary Fig. 1 (b) is monotonically decreasing and no specific feature is highlighted in the electrical spectrum of Supplementary Fig. 1 (c). Further increase of the feedback strength to 10.8 ns^{-1} triggers a first kind of switching dynamics in the output of the laser, as one can observe in Supplementary Fig. 1 (d). Switching dynamics correspond to a train of pulses, as opposed to the pulsing dynamics shown in the main text for arrays of lasers. Each train of pulses is composed of many pulses, and the overall behavior is periodic. As mentioned, we found no single pulsing configuration for the lone laser under external optical feedback. The typical phase behavior of switching dynamics, shown in Supplementary Fig. 1 (e), is also very different from the phase behavior during pulsing, which will be discussed in an upcoming figure. Phase increases in steps during the pulse train and then abruptly decreases outside the pulse train, with a diminution over several periods. The electrical spectrum in Supplementary Fig. 1 (f) comprises several broad components of discrete peaks. The interval between these multiple peaks corresponds to the repetition frequency of the switching dynamics. The oscillation frequency within the switching dynamics corresponds to the maximum of the electrical spectrum. From this feedback strength value, a slight increase tunes the switching dynamics, as visualized in Supplementary Fig. 1 (g). The laser output still displays a train of pulses, but the number of pulses within the train has increased, and the amplitude of the pulses is more consistent. The evolution of phase in Supplementary Fig. 1 (h) underscores that the two switching dynamics share similar features, and that confirms the difference with pulsing dynamics. The electrical spectrum shown in Supplementary Fig. 1 (i) does not differ much from that shown in Supplementary Fig. 1 (f), but each peak is broadened. A wide variety of switching dynamics (not shown here) can be obtained when varying κ^f around 11-14 ns^{-1}. When the feedback strength is increased, the train of pulses contains more and more pulses until it becomes continuous, and only the fast oscillation remains. Such state can be observed in Supplementary Fig. 1 (j) for $\kappa^f = 17$ ns^{-1}. The phase decreases over long time scales and otherwise follows the oscillation pattern at short time scales, as seen in Supplementary Fig. 1 (k). The electrical spectrum in Supplementary Fig. 1 (l) contains the frequency component related to the oscillation frequency and several harmonics of the main frequency. Each contribution is narrow-band, contrasting with the electrical spectra for switching dynamics. In this single-laser configuration, intermediate feedback strength can also lead to low-complexity chaos dynamics, and this is illustrated in Supplementary Fig. 1 (m) for $\kappa^f = 25$ ns^{-1}. The phase in Supplementary Fig. 1 (n) now decreases much faster with time and shows small amplitude fluctuations that seem to retain an almost periodic behavior with a typical scale close to roundtrip time (3 ns). The electrical spectrum in Supplementary Fig. 1

(o) displays a wide component, which is a typical feature of chaos dynamics, but discrete peaks can still be found within the structure, hence explaining why the temporal pattern of Supplementary Fig. 1 (m) belongs to low-complexity chaos.

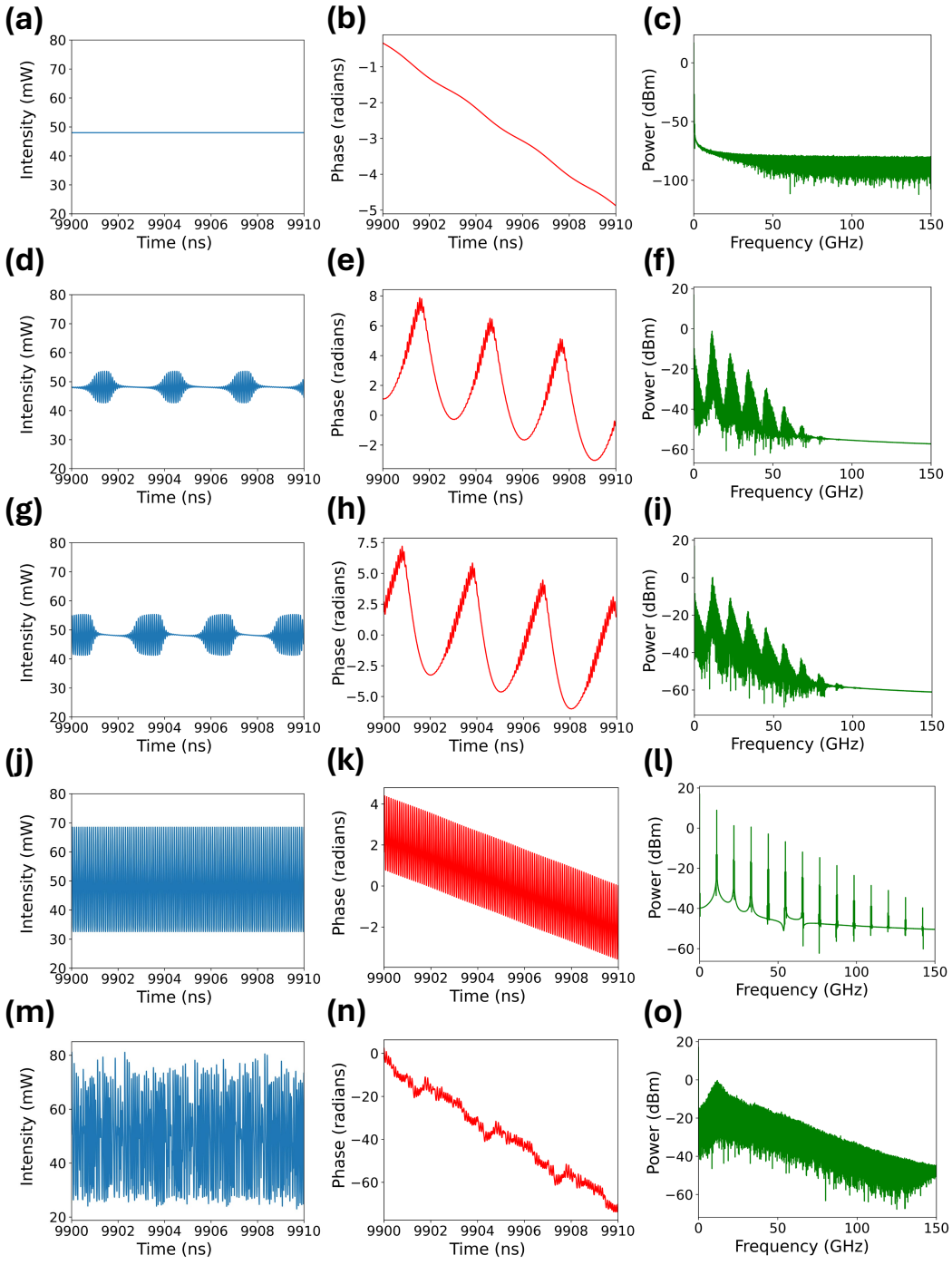

Supplementary figure 1. Nonlinear dynamics that can be observed for a bias current high above threshold ($\beta = 7$) and several conditions of feedback strength in a single laser; (a) Intensity time trace, (b) phase time trace, and (c) electrical spectrum for $\kappa^f = 10$ ns^{-1}, illustrating steady-state dynamics at low feedback strength; (d-f) identical to (a-c) but for $\kappa^f = 10.8$ ns^{-1}, corresponding to a first type of switching dynamics; (g-i) identical to (a-c) but for $\kappa^f = 11$ ns^{-1}, corresponding to a second type of switching dynamics; (j-l) identical to (a-c) but for $\kappa^f = 17$ ns^{-1}, corresponding to fast oscillations in the output of the laser; (m-o) identical to (a-c) but for $\kappa^f = 25$ ns^{-1}, corresponding to low-complexity chaos dynamics. The frequency detuning for this laser is 0. Other parameters not mentioned here are as shown in Supplementary Table. 1

Default parameters for the Lang-Kobayashi model simulations

The Lang-Kobayashi model in the context of an array of semiconductor lasers takes into account various dynamical parameters that we list in this section, and the values for each parameter used in the 30 laser models of the main text are gathered in Supplementary Table 1. The relationship between the threshold current J_{th}, defined as a number of electrons per unit of time (used in the equations) and I_{th}, the threshold current in unit of A (described in the table) is $J_{th} = \frac{I_{th}}{e}$, with e the charge of an electron. The external cavity time delay is held constant across all lasers in the simulations presented. While we also computationally verified the persistence of pulsing dynamics in the presence of disordered time delays, we focus here on non-disordered configurations to better elucidate the underlying mechanism and facilitate comparison with the reduced models. Supplementary Table 2 lists the frequency detuning parameters used in the 30-laser Lang-Kobayashi model, corresponding to the simulation results presented in Supplementary Fig. 2. This is similar to the 30 laser model mentioned in the main text, but with the addition of random variation in the frequency detuning values. Supplementary Table 3 shows the parameters used in the two-laser Lang-Kobayashi model, whose simulation results are shown in Fig. 4(a) in the main text.

Supplementary table 1. Details of the parameters for simulating the 30-Lang-Kobayashi laser model array. The values used in the simulations are compatible with those usually found in semiconductor lasers.[3,4]

Symbol	Description	Value
λ	Wavelength	770 nm
α	Linewidth enhancement factor	5.0
g	Differential gain coefficient	1.5×10^{-5} ns^{-1}
s	Gain saturation coefficient	2×10^{-7}
γ	Cavity loss	500 ns^{-1}
N_0	Carrier number at transparency	1.5×10^{8}
γ_n	Carrier loss rate	0.5 ns^{-1}
$f_{odd} = \omega_{odd}/2\pi$	Frequency detuning for odd lasers	-2 GHz
$f_{even} = \omega_{even}/2\pi$	Frequency detuning for even lasers	2 GHz
τ	Feedback delay time	3 ns
κ^f	Feedback strength	varied
d	Cross-laser reinjection efficiency	0.75
β	Pump factor	7.0
I_{th}	Threshold pump current for a single laser	14.7 mA

Perturbation of the frequency detuning in the 30-laser configuration

The main manuscript details the pulsing dynamics in an array of 30 lasers with frequency detuning. To optimize the pulsing dynamics, which includes the juxtaposition of anti-phase and in-phase synchrony, we focused on a configuration with a frequency detuning of -2 GHz for odd lasers and 2 GHz for even lasers. However, this requirement can be relaxed without significantly impacting the observed dynamics. With the frequency detuning values listed in Supplementary Tab. 2, one can observe the pulsing dynamics displayed in Supplementary Fig. 2, among others. A configuration with a single pulse per period is illustrated in Supplementary Fig. 2 (a) for the full array of 30 lasers, and the alternate behavior between the even and the odd lasers is still observed. In Supplementary Fig. 2 (b) the phase time trace for an even and an odd laser shows that the phase behavior strongly differs compared to what was described in Supplementary Fig. 1 for a single laser. The phase is overall decreasing and there is a positive step every time a pulse is triggered for the even lasers while there is a negative step every time a pulse is triggered for the odd lasers. The synchrony behavior is detailed in Supplementary Fig. 2 (c) and shows again that anti-phase synchrony is followed by in-phase synchrony. Pulsing in the odd lasers aligns with the anti-phase behavior, while pulsing in the even lasers coincides with the in-phase behavior. We also highlight a case with two pulses per period, as seen in Supplementary Fig. 2 (d). The phase time trace in Supplementary Fig. 2 (e) confirms that the number of steps is related to the number of pulses, as two steps per period can be observed. The last panel, meaning Supplementary Fig. 2 (f), showcases the synchrony features already observed without the perturbation of the frequency detuning. Overall, this example underscores that the frequency detuning does not need to be strictly -2 or 2 GHz to observe pulsing and an uncertainty of more than 0.1 GHz can be tolerated for some lasers in the array. This finding is noteworthy as it can be complex to experimentally manufacture an array of lasers with extremely precise frequency detuning. A typical uncertainty of 0.1 GHz can be achieved more realistically and should not impact the pulsing phenomenon. This alternating configuration of detuning values was engineered to encourage

Supplementary table 2. Frequency detuning values for the 30-lasers array in the perturbed detuning case.

Laser number	Frequency detuning (GHz)
1	-2.059
2	2.008
3	-2.079
4	1.887
5	-1.998
6	2.117
7	-2.041
8	2.035
9	-1.930
10	2.008
11	-1.952
12	2.155
13	-1.781
14	2.020
15	-2.178
16	2.033
17	-1.982
18	1.893
19	-1.998
20	2.032
21	-1.883
22	2.011
23	-2.108
24	2.128
25	-2.016
26	2.068
27	-1.978
28	2.072
29	-2.028
30	2.017

pulsing, but pulsing can be achieved with other non-alternating configurations, as demonstrated in the next section.

Example with sparse frequency detuning configuration

In addition to the perturbed frequency detuning that is underscored in the previous section, pulsing was achieved in an example with a non-alternating detuning configuration. This example has an array of 20 lasers, and its behavior is illustrated in Supplementary Fig. 3. The frequency detuning on lasers 5, 10, and 15 is 4 GHz. All other lasers have a detuning of zero. Other parameters are the same as those shown in Supplementary Tab. 1. Pulsing has the greatest amplitude on the three lasers with 4 GHz detuning. The amplitude of the pulses is weaker for lasers farther from these detuned lasers, with the lasers on the edges showing the lowest amplitude pulses. This further proves that pulsing is driven by differences in frequency detuning between lasers in an array. The synchrony behavior shows anti-phase synchrony followed by in-phase synchrony, as seen in Supplementary Fig. 3(c) and (f), although neither is as pronounced as in the alternating-detuning cases.

Computational support for deriving the reduced model

The objective of the reduced model is to explain the origin of the pulsing behavior in the minimum network required to generate pulsing, which is a network of two lasers with transverse coupling. The parameters used in the two-laser model shown in Fig. 4(a) of the main text are summarized in Supplementary Tab. 3. To derive the reduced model, we approximate $r_1(t-\tau) \approx r_1(t) \approx r_2(t-\tau) \approx r_2(t)$, $\phi_i(t-\tau) \approx \phi_i(t)$, and $N_1(t-\tau) \approx N_1(t) \approx N_2(t-\tau) \approx N_2(t)$. To demonstrate the validity

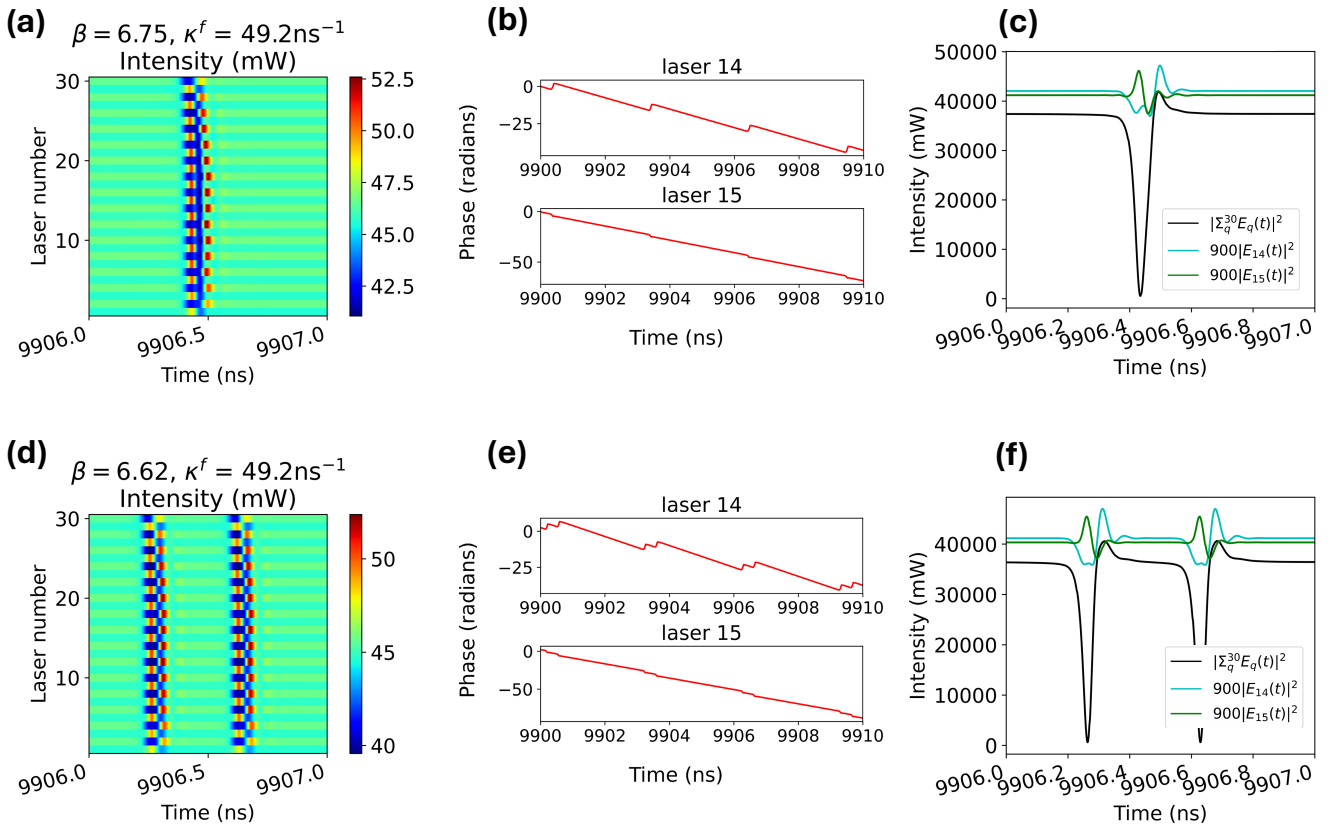

Supplementary figure 2. Robustness of pulsing dynamics in a 30-laser array under perturbed frequency detuning. Investigation of a 30-laser pulsing case similar to the one highlighted in the main text, but with the addition of perturbed frequency detuning. (a) Single-pulsing dynamics in the array of 30 lasers, with the odd and even-numbered lasers showing alternate behaviors. (b) Phase time traces for one selected odd-numbered laser and one selected even-numbered laser, both showing a sharp phase step at the instant of pulsing that contrasts with the otherwise linear evolution of the phase. (c) Combined field intensity (black curve) of the 30 lasers in the array, illustrating when the lasers are anti-phase synchronized and in-phase synchronized. Also shown are the magnified intensities of an odd-numbered laser (green curve) and an even-numbered laser (cyan curve). (d-f) Same as panels (a-c) but for a configuration with two pulses per period.

of these approximations for the two-laser case, example plots are shown in Supplementary Fig. 4 for the pulsing case in which $\kappa^f = 18.0ns^{-1}$ and $\Delta\omega = 3.0GHz$.

The normalized differences between the non-delayed and time-delayed versions of $r_2(t)$, $\phi_2(t)$, and $N_2(t)$ are plotted in Supplementary Fig. 4(a). The absolute value of $(\phi_2(t) - \phi_2(t-\tau))/\phi_2(t)$ is below 5×10^{-5} for all time, and remains below 1.2×10^{-5} between pulses. The absolute value of $(N_2(t) - N_2(t-\tau))/N_2(t)$ is below 0.02 for all time and remains below 2×10^{-6} between pulses. The absolute value of $(r_2(t) - r_2(t-\tau))/r_2(t)$ is slightly larger, at a maximum around 0.2, but remains below 1×10^{-5} between pulses. This maximum value may be due to a period that differs slightly from τ or small differences in pulse shapes. The fact that all these values remain around zero for most of the time supports the approximations $r_2(t-\tau) \approx r_2(t)$, $\phi_2(t-\tau) \approx \phi_2(t)$, and $N_2(t-\tau) \approx N_2(t)$. The same trends hold true for laser 1, so $r_1(t-\tau) \approx r_1(t)$, $\phi_1(t-\tau) \approx \phi_1(t)$, and $N_1(t-\tau) \approx N_1(t)$.

The normalized differences between the $r_i(t)$ and $N_i(t)$ values for the two lasers are shown in Supplementary Fig. 4(b). The absolute value of $(N_2(t) - N_1(t))/N_2(t)$ is below 0.025 for all time, and remains below 4.1×10^{-3} between pulses. The absolute value of $(r_2(t) - r_1(t))/r_2(t)$ is slightly larger, at a maximum under 0.2, but remains below 0.013 between pulses. As before, the fact these values are generally around zero validates the approximation $r_1(t) \approx r_2(t)$ and $N_1(t) \approx N_2(t)$.

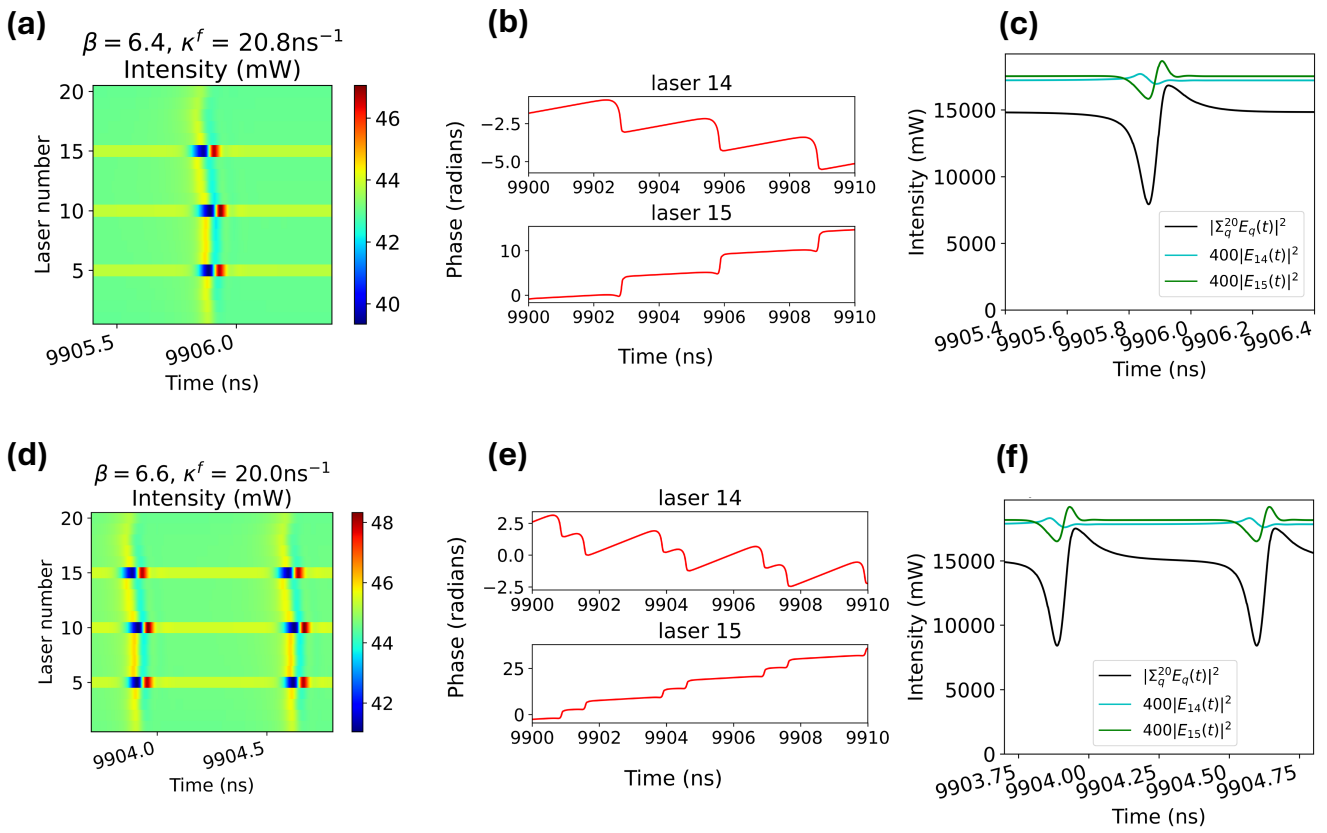

Supplementary figure 3. Investigation of a 20-laser pulsing case when a limited number of emitters in the array exhibit frequency detuning, with only $\omega_5 = \omega_{10} = \omega_{15} = 4$ GHz being non-zero. (a) Overview of single pulsing in the array of 20 lasers. (b) Phase time trace for laser #14 and laser #15, both showing a step at the instant of pulsing that contrasts with the otherwise linear evolution of the phase. (c) Combined field intensity (black curve) of the 20 lasers in the array, illustrating when the lasers are anti-phase synchronized and in-phase synchronized. This panel also shows the magnified intensity of laser #14 (cyan curve) and the magnified intensity of laser # 15 (green curve). (d-f) similar to (a-c) but for a configuration with two pulses per period.

Supplementary table 3. Details of the parameters for simulating the two-Lang-Kobayashi laser model array.

Symbol	Description	Value
λ	Wavelength	770 nm
α	Linewidth enhancement factor	2.5
g	Differential gain coefficient	1.5×10^{-5} ns^{-1}
s	Gain saturation coefficient	2×10^{-7}
γ	Cavity loss	500 ns^{-1}
N_0	Carrier number at transparency	1.5×10^8
γ_n	Carrier loss rate	0.5 ns^{-1}
ω_1	Frequency detuning for laser 1	-$\Delta\omega/2$
ω_2	Frequency detuning for laser 2	$\Delta\omega/2$
τ	Feedback delay time	8 ns
κ^f	Feedback strength	varied
d	Cross-laser reinjection efficiency	1.0
β	Pump factor	9.0
I_{th}	Threshold pump current for a single laser	14.7 mA

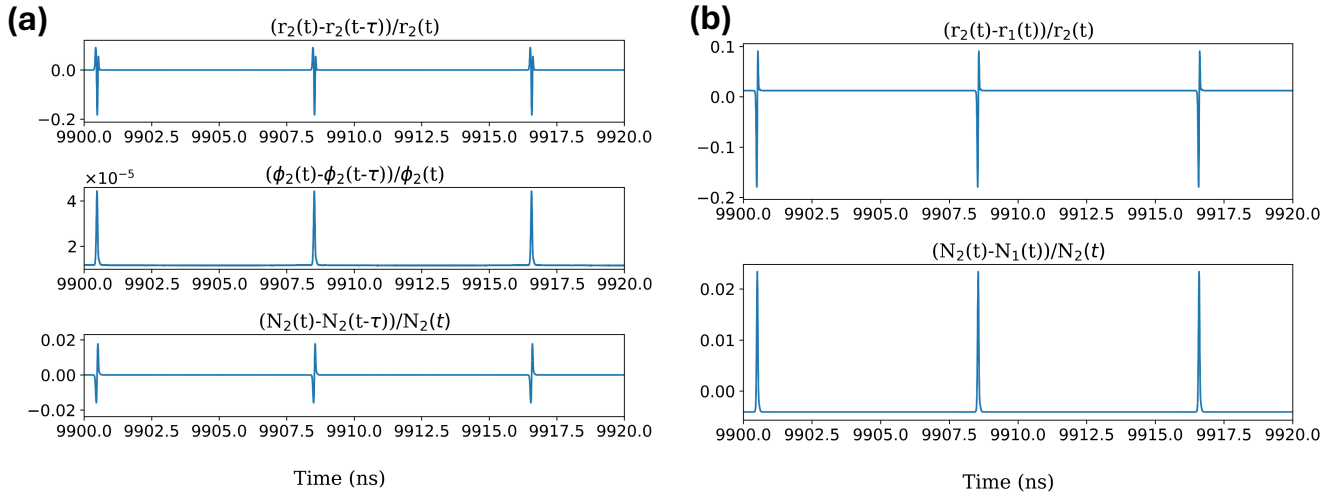

Supplementary figure 4. Plots demonstrating the validity of the approximations used for the reduced model. These are shown for the two-laser full Lang-Kobayashi model simulations for the pulsing case in which $\kappa^f = 18.0ns^{-1}$ and $\Delta\omega = 3.0GHz$. (a) normalized differences between non-delayed and time-delayed versions of $r_2(t)$, $\phi_2(t)$, and $N_2(t)$. (b) normalized differences between the $r_i(t)$ and $N_i(t)$ values for the different lasers.

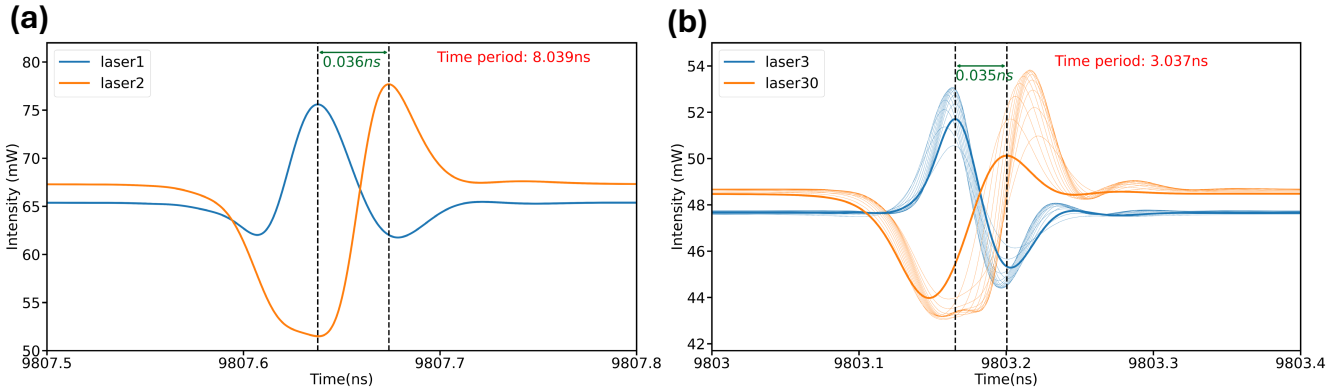

Supplementary figure 5. Time difference between the pulsing of the odd and even lasers. **(a)** Two coupled lasers: The time difference between the pulsing of the odd and even lasers is illustrated in the time series of intensities for two coupled lasers. The blue solid line represents the intensity of the first laser, while the orange solid line represents the intensity of the second laser. The black vertical dashed lines indicate the pulse timing for the first and second lasers. The time window between these pulses is approximately 0.036 ns. The total time period between pulsing events for the array is approximately 8.039 ns, slightly longer than the feedback delay time of $\tau = 8$ ns, indicating that the additional time unaccounted for, is approximately 0.039 ns. This is very close to the time difference between peaks in intensity for laser 1 and laser 2, as previously mentioned, 0.036 ns. The parameters are set as follows: $\Delta f = 3.5$ GHz, $\kappa^f = 19.5\text{ns}^{-1}$, with all other parameters as described in Supplementary Table 3. **(b)** 30 laser array: The odd and even groups are represented by blue and orange lines, respectively. Laser #3 and Laser #30 are depicted by bold lines. In terms of pulse timing, Laser #3 is the last laser in the odd group, while Laser #30 is the first laser in the even group. The time difference between the pulses of Laser #3 and Laser #30 is approximately 0.035 ns, which is very close to the additional time (≈ 0.037 ns) in the time period for this case. The parameters used are the same as those in Fig. 2(b) of the main text.

Supplementary References

1. Masoller, C. Spatiotemporal dynamics in the coherence collapsed regime of semiconductor lasers with optical feedback. Chaos: An Interdisciplinary Journal of Nonlinear Science 7, 455–462 (1997).

114 **2.** Dong, J.-X. Ruan, J. Zhang, L. Zhuang, J.-P. & Chan, S.-C. Stable-unstable switching dynamics in semiconductor lasers
115 with external cavities. Physical Review A 103, 053524 (2021).

116 **3.** Liu, B. Braiman, Y. Nair, N. Lu, Y. Guo, Y. Colet, P. & Wardlaw, M. Nonlinear dynamics and synchronization of an array of
117 single mode laser diodes in external cavity subject to current modulation. Optics Communications 324, 301–310 (2014).

118 **4.** Nair, N. Hu, K. Berrill, M. Wiesenfeld, K. & Braiman, Y. Using disorder to overcome disorder: A mechanism for frequency
119 and phase synchronization of diode laser arrays. Physical Review Letters 127, 173901 (2021).